Journal of ELECTRONIC MATERIALS, Vol. 49, No. 8, 2020
https://doi.org/10.1007/s11664-020-08220-9

Structural and Electrical Properties of Cerium Oxides Doped by Sb^{3+} and Bi^{3+} Cations

K. SANDHYA ,[1,3] N.S. CHITRA PRIYA,[1] DEEPTHI N. RAJENDRAN,[1] and PRAVEEN THAPPILY[2]

1.—Department of Physics, Govt. College for Women, University of Kerala, Thiruvananthapuram, India. 2.—Department of Electronics, E.S.P.I.R.T. Industries, Redon, France. 3.—e-mail: sandhyakprabeesh@gmail.com

The addition of low melting point trivalent ions in ceria-based electrolyte systems results in a new composite with better oxygen ion conduction at reduced temperature. The present work discusses the synthesis and characterization of co-doped ceramic electrolyte $Ce_{0.8}Sm_{0.1}M_{0.1}O_{2-\delta}$ (M = Bi, Sb) prepared by coprecipitation. This study mainly focuses on the effect of the ionic radius of the dopants on the structural and electrical properties of doped ceria. The structural studies of the samples by X-ray diffraction, field emission scanning electron microscopy and transmission electron microscopy show nanosized particles with a cubic fluorite structure. Raman spectroscopy confirmed the presence of O^{2-} vacancies introduced into the lattice due to the substitution of a large ionic radius of Bi^{3+} for Ce^{4+}. The electrical survey by electrochemical impedance spectroscopy suggests that the dopant ionic radius has a significant influence on the ionic conductivity and activation energy of the doped ceria. There is an enhancement in conductivity noted for bismuth-co-doped samarium-doped ceria due to the larger ionic radius of the bismuth dopant compared to antimony-co-doped samarium-doped ceria.

Key words: Electrolyte, ionic radius, coprecipitation method, electrical properties

INTRODUCTION

A solid oxide fuel cell (SOFC) is a clean energy solid state device with dense oxygen ion conducting ceramic membrane as the electrolyte. The electrolyte is the main component in determining the performance of SOFCs.[1,2] The study of CeO_2 -based electrolyte material occupies an active area of research. In most of the research work, the ideal characteristics required for the electrolyte material are satisfied by certain ceramics with fluorite or perovskite structure. Most materials used include yttria-stabilized zirconia (YSZ) [3,4] and gadolinium-doped ceria (GDC),[5–7] both with a fluorite-type structure. But a major underlying problem in the CeO_2 -based electrolyte material research is the high temperature required to obtain adequate oxide ion conduction. These drawbacks spurred research on the search of compositions as are necessary for better electrolytes with high density and good ionic conductivity.

Rare earth oxides possess high solubility in ceria. However, the reduction of Ce^{4+} to Ce^{3+} at temperatures higher than 600°C poses a significant problem for its use. The mechanical properties of the cell are mainly affected by the reduction of ceria due to lattice expansion. Improper mechanical stability is the major problem faced by samarium-doped ceria (SDC)-based SOFC. The co-doping method has been adopted to resolve the issue of mechanical stability and enhance the ionic conductivity in CeO_2. The co-doping process was done by choosing one dopant with a radius less than ceria and another dopant whose is radius greater. As a result, expansion and

(Received July 6, 2019; accepted May 13, 2020; published online May 27, 2020)

contraction of the CeO_2 lattice are balanced out, resulting in better ionic conductivity.[8] Solubility is the main factor limiting the doping process. There is contradicting information from the literature regarding the solubility of large and small rare earth dopants. The work on Sc^{3+} -doped samples reported that the samples exhibit solubility limits up to 3–5% mole dopant fraction. Further studies on large dopants such as La^{3+} explored the solid solution of $Ce_{0.8}La_{0.2}O_{1.9}$ samples showing that they are metastable, and complete solubility was obtained after prolonged sintering for 7 days at high temperature. These studies report that the lattice parameter and ionic conductivity strongly depends on the ionic radius of the dopant. It is important to note that the small ionic radius dopants show a decrease in the lattice parameter and lower grain boundary conductivity up to certain doping percentage. In contrast to smaller dopants, the large dopants marked an increase in the lattice parameter and low bulk conductivity constrained to a certain doping percentage. But there is earlier work that reported deviations from Vegard's law due to the association of oxygen vacancies with dopants.[9]

It is interesting to investigate the effect of radii and activation enthalpies of Sb^{3+} and Bi^{3+} on the conductivity of ceria. The effective enthalpies are usually composed of association enthalpy H_a and migration enthalpy H_m. Activation enthalpies of the prepared samples are obtained from the Arrhenius plot. The difference in the ionic radii of the dopants and host cations generates oxygen vacancies depending on the nature and amount of the dopant.[10,11] In the present investigation, a series of rare earth-doped cerium oxides have been prepared using wet coprecipitation. Wet coprecipitation is done in an alkaline medium. The pH of the precursor solution determines the shape of the prepared nanomaterial. The main aim of the work is to see the effect of the dopant's ionic radius and activation enthalpy on the structural and electrical properties of nanoceria prepared by wet chemical methods.

EXPERIMENTAL

A series of rare earth co-doped cerium oxide nanomaterials $Ce_{1-x}Sm_{x-y}M_yO_{2-\delta}$ (M = B, Sb and Bi, $x = 0.2$ and $y = 0$, 0.1) were prepared using coprecipitation. A stoichiometric amount of high purity (99.9%) nitrates were separately dissolved in 20 ml of distilled water and mixed in a beaker. The homogenous solution of the mixture was obtained by continuously stirring using a magnetic stirrer for 2 h. The pH of the solution was regulated to 9 with the dropwise addition of ammonia. The mixture was filtered and washed, and the precipitate was dried in a hot air oven. The powders are then calcined at 400°C for 2 h. A small weight percentage of polyvinyl alcohol (PVA) was added as a binder to the calcined powder. Then the calcined powder was pressed into a pellet of 12-mm diameter and around 2–3 mm thickness under a pressure 100 kg/cm^2. The 20SDC, 10S10SbDC, and 10S10BiDC pellets were sintered at temperatures 1200°C for 4 h, 800°C for 4 h, and 850°C for 4 h, respectively. The structural measurements of the samples were performed using a Bruker AXS D8 Advance X-ray powder diffractometer with an incident Cu-Kα radiation of 1.5406 Å. Field emission scanning electron microscopy (FESEM) of sintered samples was carried out using a Model JSM - 6390LV electron microscope. Transmission electron microscopy (TEM) of the sintered samples was done using a Jeol/JEM 2100 electron microscope with a LaB6 source operating at 200 kV. The microscopic images are obtained at different resolutions along with the SAED pattern. Raman spectroscopy measurement was carried out using a Raman spectrometer (EZRaman, Enwave Optronics). The excitation wavelength used for the sample was 785 nm and measured in the range 100–3000 cm^{-1}. The electrical properties of solid electrolytes were measured using electrochemical impedance spectroscopy Solatron 1260A.

RESULTS AND DISCUSSION

XRD Analysis

Figure 1 shows the X-ray diffraction (XRD) pattern of the doped samples. The room temperature XRD pattern shows that all the three doped samples exhibit a cubic fluorite structure with Fm $\bar{3}$ m space group. The absence of secondary phases is confirmed through Rietveld refinement using Fullprof suite software. The lattice parameter of pure ceria is noted to be 5.411 Å from the ICDD file (34-0394). A broadening of the peak is indicated for the doping of trivalent elements due to the larger ionic radius of the dopant cation compared to that of the host cation (Ce^{4+}). It is noted that the larger Bi^{3+} (1.21 Å) substituted in the place of Ce^{4+} (0.97 Å), and the lattice expands according to Vegard's law. But the doping of Sb^{3+} indicated contraction in the lattice due to the smaller ionic radius of Sb^{3+} (0.76 Å) compared to that of Ce^{4+} (0.97 Å). As a result, the lattice contracted and did not dilate because of Sb^{3+} doping.[12–15] The results of Rietveld refinement are tabulated in Table I.

Microstructural Analysis

Microstructural features within the structures are identified using Fig. 2. 20SDC samples exhibit a dense structure with uniform particles, and consequently better packing. A high-density value is obtained for 20SDC sintered at 1200°C for 4 h. On the other hand, 10S10BiDC pellets sintered at 850°C for 4 h show a closely packed structure with non-uniform particles and a small amount of SiO_2 impurities. These impurities accumulate at the

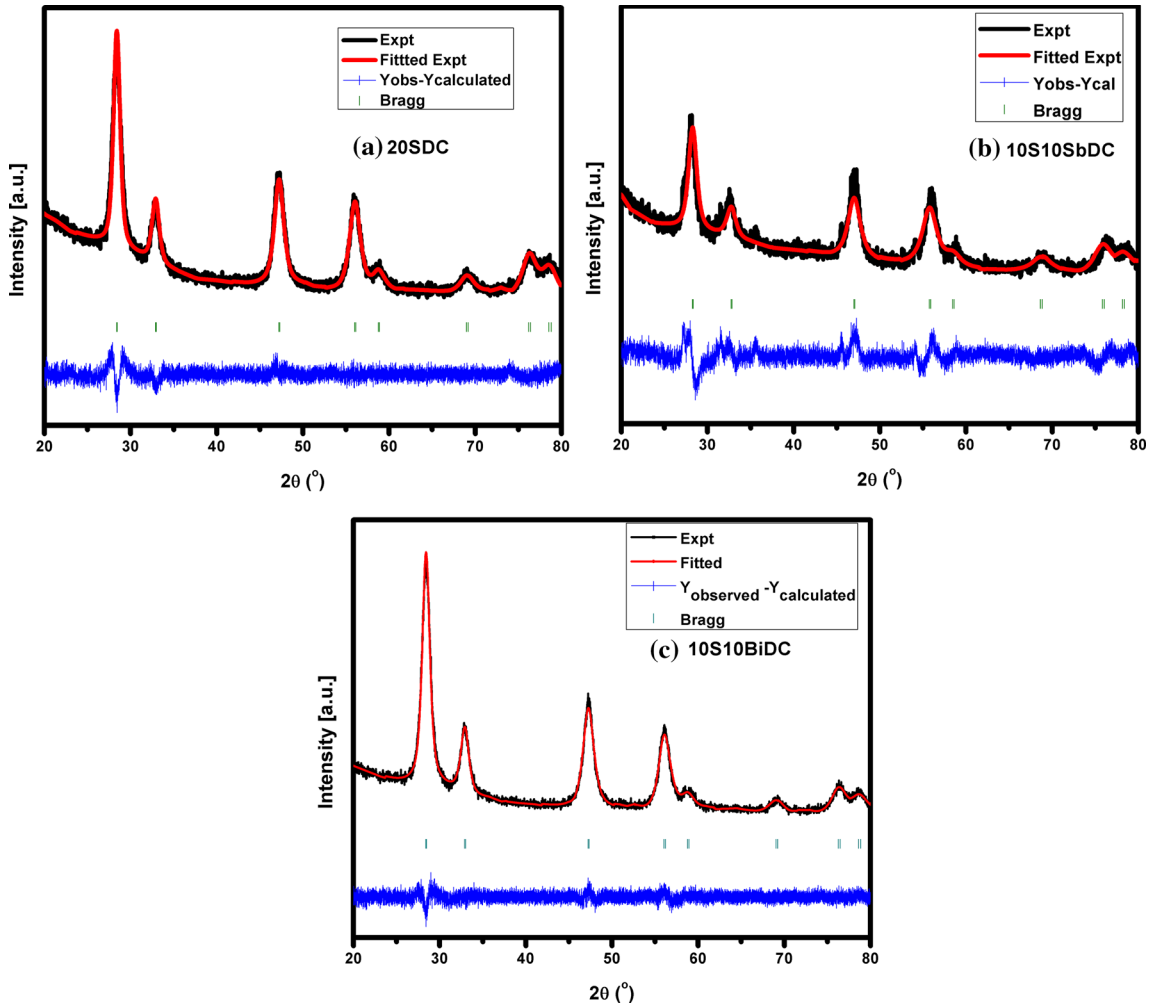

Fig. 1. Reitveld refinement of (a) $Ce_{.8}Sm_{.2}O_{2-\delta}$ (20SDC), (b) $Ce_{.8}Sm_{.1}Sb_{.1}O_{2-\delta}$ (10S10SbDC) and (c) $Ce_{.8}Sm_{.1}Bi_{.1}O_{2-\delta}$ (10S10BiDC) samples.

Table I. illustrates lattice parameters, crystallite size, volume, goodness-of-fit (Chi^2) obtained after Rietveld refinement

Sample names	Composition	Lattice parameter (Å)	Crystallite size	Volume V((Å)3)	Chi^2
20SDC	$Ce_{0.8}Sm_{0.2}O_{2-\delta}$	5.430	11.676	161.676	1.59
10S10SbDC	$Ce_{0.8}Sm_{0.1}Sb_{0.1}O_{2-\delta}$	5.276	21.991	146.848	2.61
10S10BiDC	$Ce_{0.8}Sm_{0.1}Bi_{0.1}O_{2-\delta}$	5.436	14.768	160.651	1.38

grain boundaries and form an amorphous siliceous layer. The closely packed structure is attributed to better ionic conductivity. Micrograph images of 10S10SbDC pellets sintered at 800°C for 4 h indicate the presence of mesopores and micropores. The densification process is slowed due to the appearance of pores resulting in less compact particle packing.

Density is an important parameter that determines the ionic conductivity of the pellets. Pore size distribution and particle size of the sintered pellet plays a significant role in obtaining high density. The theoretical density was calculated using the geometrical mass and dimension of the sintered pellet (Table II). The Archimedes principle measured the bulk density of sintered pellets.

$$\rho_{T=\frac{\rho_s}{\rho_{Th}}\times 100} \quad (1)$$

where ρ_s and ρ_{Th} denote bulk density and theoretical density, respectively.

Transmission Electron Microscopy Analysis

The TEM images of the three sintered pellets are shown in Fig. 3. The TEM images show agglomerated sheets and clusters of individual crystallites.

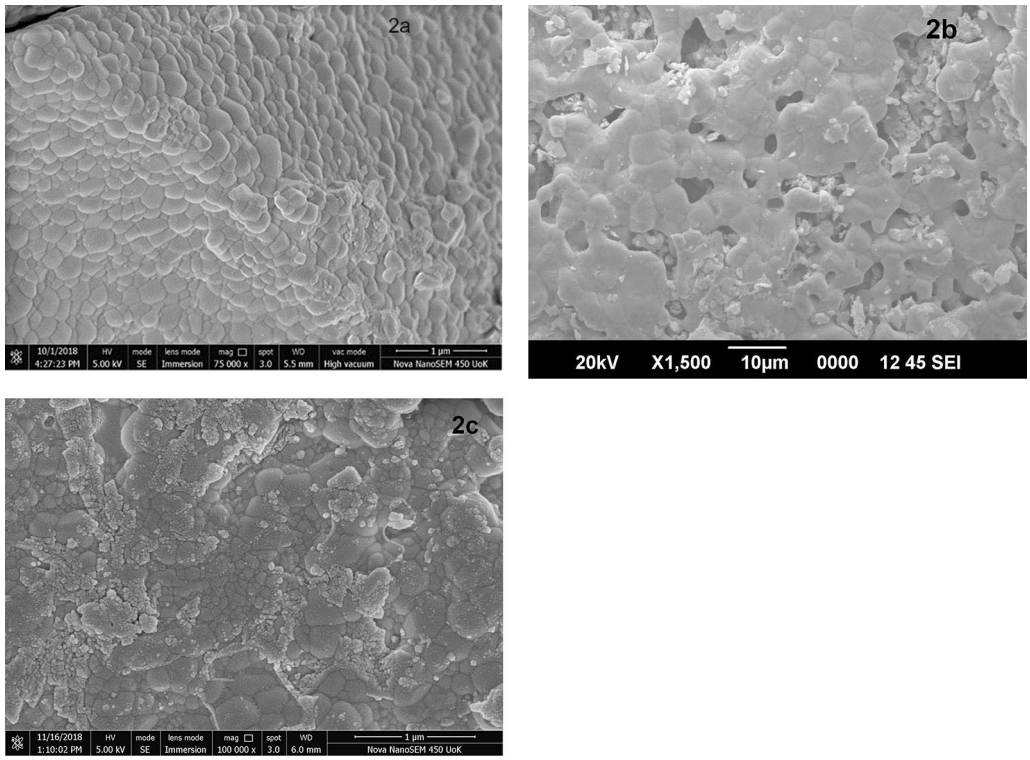

Fig. 2. SEM images of (a) 20SDC, (b) 10S10SbDC and (c) 10S10BiDC sintered pellets.

Table II. demonstrate the bulk density and theoretical density of the sintered pellets

Composition	Theoretical density (g/cm^3)	Bulk density (g/cm^3)	Relative density (%)
$Ce_{0.8}Sm_{0.2}O_{2-\delta}$	7.16	6.80	95.02
$Ce_{0.8}Sm_{0.1}Sb_{0.1}O_{2-\delta}$	7.65	6.14	80.31
$Ce_{0.8}Sm_{0.1}Bi_{0.1}O_{2-\delta}$	7.38	6.88	93.21

The XRD pattern of the three doped samples is indexed to the cubic fluorite structure. SAED patterns of the sintered pellets confirm the results obtained by XRD. SAED patterns have high- resolution lattice fringes, which indicate the particles are clean, visually free of impurities, and single crystalline structure. The single crystalline structure confirmed from the lattice fringes marked according to the reflections obtained in the SAED pattern.[17–19]

Raman Spectroscopy Analysis

Raman Spectroscopy is a useful technique to study the O^{2-} vacancies in solid electrolytes based on CeO_2. It is reported from the previous work that the Raman mode positioned at 465 cm^{-1} corresponds to the pure and stoichiometric CeO_2 with fluorite structure.[20] Apart from that mode, there is an additional mode appearing at 550 cm^{-1} and 600 cm^{-1} in Fig. 4 confirmed retention of oxygen vacancies in the ceria lattice in 20SDC and 10S10BiDC sintered pellets.[21] The presence of oxygen (O^{2-}) vacancies is indicated by the presence of a peak at 550 cm^{-1} and 600 cm^{-1}. This defect band is formed due to the generation of an oxygen vacancy as the dopant cation is substituted in CeO_2 to neutralize the charge compensation effect. The weak intensity peak noted at 550 cm^{-1} and 600 cm^{-1} indicate the lower concentration of O^{2-} vacancies in the 10S10SbDC sintered pellet.

Electrochemical Impedance Spectroscopy Analysis

In the electrochemical impedance spectroscopy (EIS) analysis, the Nyquist plot contains three arcs, high frequency, middle frequency, and low frequency tails, which arise from bulk, grain, and boundaries and electrode processes.[22] In most of the Nyquist plot, the arcs cannot all be displayed due to the constrained frequency range of the instrument and applied temperatures. The electrical studies of the sintered pellets are carried out, and the properties are measured using electrochemical impedance spectroscopy. Figure 5 shows the

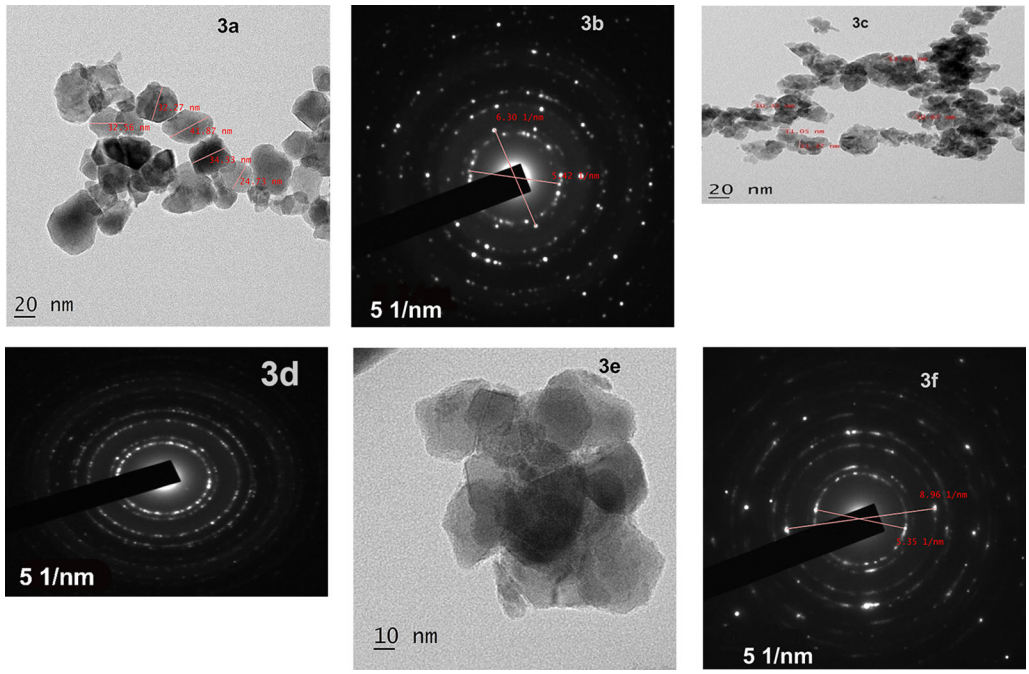

Fig. 3. TEM images of (a) 20SDC, (c) 10S10SbDC and (e) 10S10BiDC, and SAED pattern of (b) 20SDC, (d) 10S10SbDC and (f) 10S10BiDC sintered pellets.

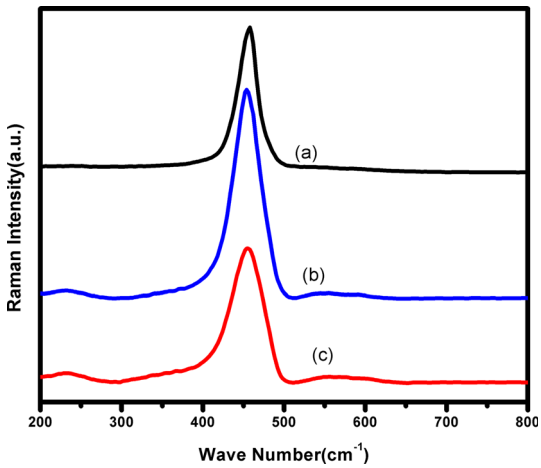

Fig. 4. Raman Spectra of (a) 10S10SbDC, (b) 20SDC and (c) 10S10BiDC sintered pellets.

Nyquist plot of three sintered pellets. The Nyquist plots are fitted using EC lab software. The fitted circuit of 20SDC,10S10SbDC, and 10S10BiDC are shown in the inset of the corresponding plots. As the temperature rises, the change in impedance and related parameters are noted for the three sintered pellets. Above 400°C and 500°C, two well-defined semicircles are visible, one at high and other at low frequency for 20SDC and 10S10BiSDC. In the case of 20SDC and 10S10BiDCsamples, the high-frequency semicircle is considered as a parallel connection of the bulk resistance (R_b) of crystallite grains, and the geometric capacitance (C_b) of the sample. The low frequency semicircles contribute to the grain boundary resistance (R_{gb}) in parallel connection with the intergranular capacitance (C_{gb}). Circuit fitting values of capacitance (C_g and C_{gb}) are in picofarads and nanofarads, which indicates grain interior and grain boundary conduction taking place for 20SDC and 10S10BiDC. The value of resistance elements (R_b and R_{gb}) are in kiloohms and found to be decreasing with the increase of temperature in 20SDC and 10S10BiDC samples. The total value of $R_b + R_{gb}$ is obtained at higher temperatures with the real component of impedance in the specified frequency range.[23,24] The circuit fitted value of capacitance is in picofarads for 10S10SbDC, hence prominent grain interior conduction occurs at 500°C.

It is interesting to note that the impedance of the samples decreases with the increase in temperature, which indicates a thermally activated conduction mechanism. In the 20SDC and 10S10BiDC pellets displays an impedance plot corresponding to grain and grain boundary contribution. On the other hand, at certain temperatures, it is not possible to resolve the impedance data into grain and grain boundary contribution of the materials. This occurs due to the similar relaxation time corresponding to grain and grain boundaries. The main reason for this is the increase in mobility of charge carriers in the conduction mechanism by a low barrier effect.[25] Nyquist plot of 10S10SbDC shows a single deformed semicircle. From the plots, the result of bulk and grain conductivity cannot be easily identified. So, the total resistance is computed from the low-frequency intercept of the grain boundary effects. The overall conductivity can be evaluated using the equation

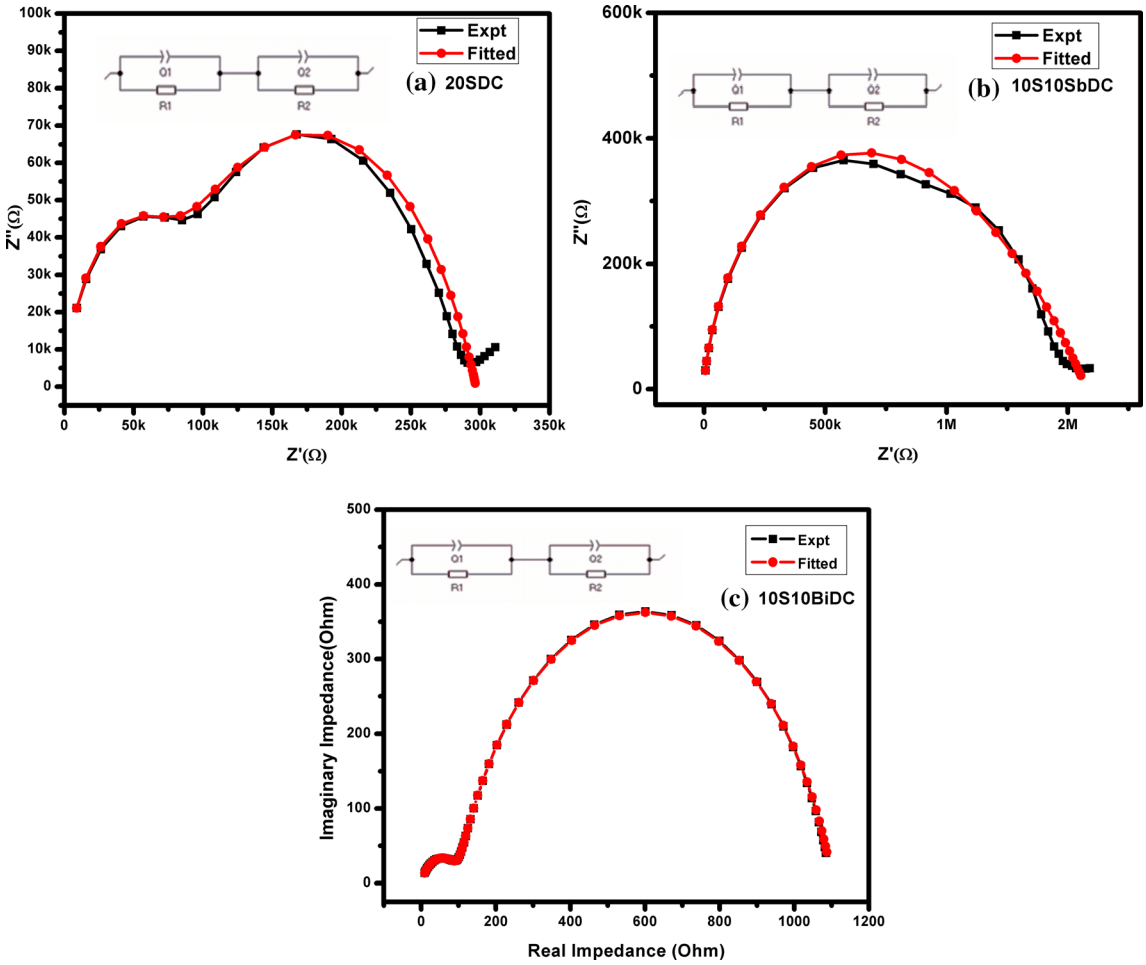

Fig. 5. The complex impedance plot of (a) 20SDC, (b) 10S10SbDC and (c) 10S10BiDC sintered pellets.

$$\sigma = \frac{l}{RA} \tag{2}$$

In which l and A represent the sample thickness and the sample electrode area, respectively.

Figure 6 shows the disparity of AC conductivity with applied frequency at different temperatures in the range 400–750°C for the sintered pellets. As the temperature increases, there is a shift in the cross-over point of the low-frequency dependent plateau and the high-frequency AC dispersive region noted in the sintered pellets. This is because with an increase in temperature, the kinetic energy of the ions also increases, and hence their vibrational frequency increases. According to the jump relaxation model, there is an increase in the hopping frequency of the carrier species with an increase in temperature. The total ionic conductivity (σ) reported in 20SDC is high, with an ionic radius that is almost the same as that of Ce^{4+} due to the minimum association enthalpy between the dopant ion and oxygen vacancy. In the 20SDC sample, it is observed that after 450°C, the high frequency dispersion end shows a tilting nature. At intermediate temperature, only a small plateau region is visible in the lower frequency side.[26,27] As the temperature increases, a static conduction region prevails in 20SDC samples, which indicates the thermally activated hopping of oxide ions. In 10S10BiDC samples, the high frequency dispersion tail vanishes after 500°C and the static conduction region marked in the sample. These changes imply that there is an increase in the migration of oxide ions with an increase in temperature. At higher temperatures (750°C) a prominent dispersion region exists in the 10S10SbDC sample. These results reveal that the thermally activated hopping of oxide ions in 10S10SbDC samples is much less than that of 20SDC and 10S10BiDC.[28]

Figure 7 displays the total conductivity ($\ln \sigma T$) as a function of inverse temperature ($1000/T$). The ionic conductivity is computed using Arrhenius relation with typical correlation coefficients for a linear least-square fit between 98.95 and 99.25.[29] The plot displays an almost linear variation of conductivity in the temperature range 400–750°C. The change in the ionic conductivity of the sintered pellet is reflected by the activation energy of the conduction. At low temperatures, the activation energy of the doped ceria system is the sum of

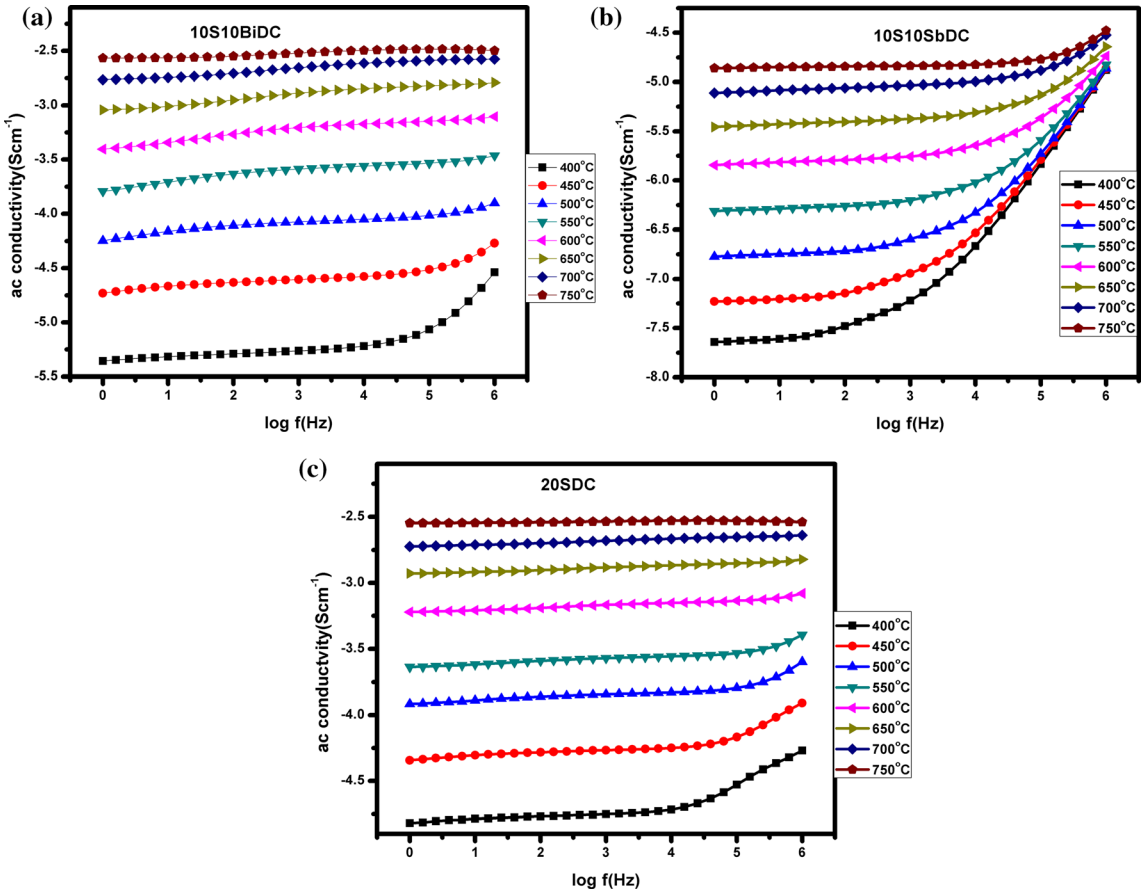

Fig. 6. AC conductivity versus frequency in the temperature range of 400–700°C of (a) 20SDC, (b) 10S10BiDC and (c) 10S10SbDC sintered pellets.

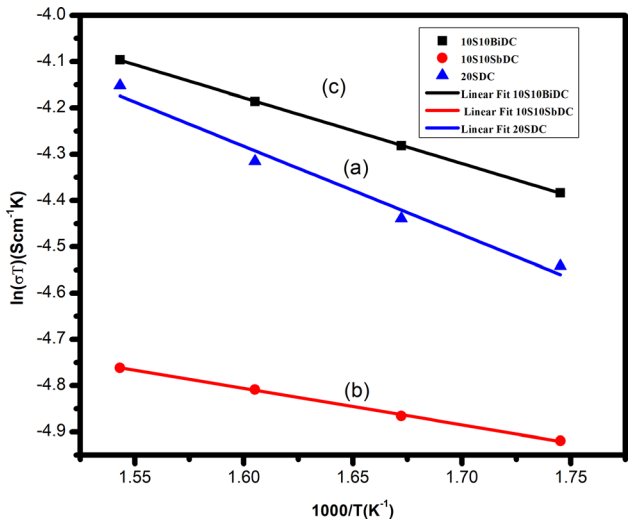

Fig. 7. Arrhenius plot of (a) 20SDC, (b) 10S10SbDC and (c) 10S10BiDC sintered pellets in the temperature range 300–475°C.

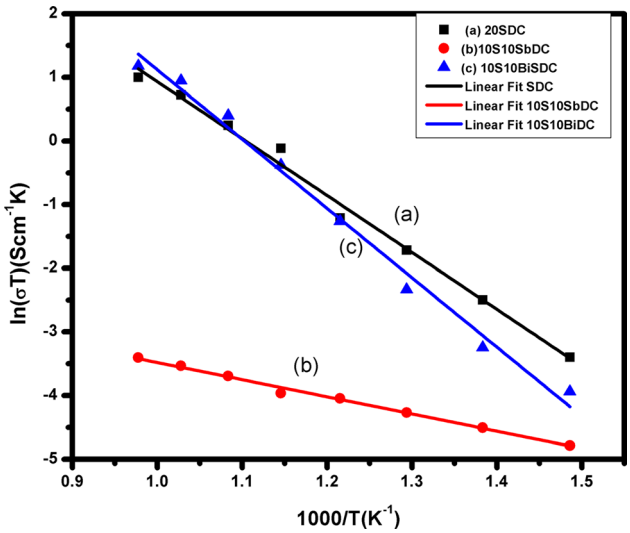

Fig. 8. Arrhenius plot of (a) 20SDC, (b) 10S10SbDC and (c) 10S10BiDC sintered pellets in the temperature range 500–750°C.

association energy (E_A) and the migration energy (E_m).[7] Association enthalpy arises due to electrostatic attraction between the dopant cations and the oxygen vacancies $[M''_{Ce} - \ddot{v}_o]$. The association enthalpy decreases the number of oxygens available for conduction. E_A also depends on the effective charge, the size of dopant, and polarizability. As the temperature increases, these associated defect pairs dissociate, and the oxygen vacancies become free. At

Table III. Activation energy, association energy and conductivity of the three sintered pellets

Sample	Compositions	Activation energy E_a (eV)		Association energy (ΔE_a/eVs)	Conductivity (Scm^{-1}) at 750°C-1 MHz frequency
		Low temp	High temp		
20SDC	$Ce_{0.8}Sm_{0.2}O_{2-\delta}$	0.92	0.77	0.15	2.66×10^{-3}
10S10SbDC	$Ce_{0.8}Sm_{0.1}Sb_{0.1}O_{2-\delta}$	0.66	0.23	0.43	3.77×10^{-5}
10S10BiDC	$Ce_{0.8}Sm_{0.1}Bi_{0.1}O_{2-\delta}$	1.1	0.95	0.13	3.18×10^{-3}

higher temperatures, therefore, migration enthalpy is the total activation energy of the system (Fig. 8). Doped fluorite oxides exhibit difference in ionic conductivity can be explained based on the activation energy for conduction. The pair binding energy contributes to the significant part of the activation energy, which depends on dopant size. The pair binding displays a minimum when $r_{host} = r_{dopant}$.[30] The total ionic conductivity (σ) reported for 20SDC is high, with an ionic radius that is almost the same the radius of Ce^{4+}(0.97 Å) due to the minimum association enthalpy between dopant ion Sm^{3+}(1.079 Å) and oxygen vacancy. Table III shows the conductivity, association energy, and activation energy of the three co-doped samples. From Table - III, the value of association energy changes for various dopants agrees with the activation energy of samarium-doped cerium oxide. Apart from the ionic radius of the dopants, association enthalpy plays a significant role in determining the ionic conductivity of doped ceria. At higher temperatures, the migration of an oxygen ion relies on the bonding/rebounding between the oxygen ion and cation and their associated enthalpies. The low value of ionic conductivity is reported for 10S10SbDC at 750°C because more energy is used for the formation of defect associates. The higher association energy is due to the segregation of small-sized cations (Sb^{3+}) at the grain boundaries. They form a positive space charge potential due to the electrons trap in the site of associates. As a result, long-range conductivity is not possible in 10S10SbDC pellets due to the decreased number of electrons at the boundaries, which hinders the flow of oxide ions. [10]

CONCLUSION

The present work emphasizes that association enthalpy and ionic radius have a remarkable impact on the conductivity and activation energy of the trivalent cation doped cerium oxides. Coprecipitation is found to be a simple and efficient method for synthesizing nanosized trivalent cation-doped cerium oxides. But the presence of a thin siliceous layer hinders the movement of oxygen ions through grain boundary resulting in lower grain boundary conductivity. The calcined powder exhibits a cubic fluorite structure. Morphological features of the sintered pellets are confirmed through FESEM and TEM analysis. Raman spectroscopy analysis confirmed the presence of O^{2-} vacancies in the trivalent cation doped cerium oxides. The thermally activated conduction process is confirmed from the impedance data. The formation of positive space charge potential due to the decreased number of electrons at the grain boundaries inhibited oxide ion conductivity in the 10S10SbDC sample. The total conductivity of the sintered pellet varies with sintering temperature in the order of 10S10BiDC > 20SDC > 10 S10SbDC at different measured temperatures. In light of comparison, 10S10BiDC has better ionic conductivity and higher density at low sintering temperatures. It is interesting to note that lower sintering temperatures resulted in better ionic conductivity, which is beneficial for their applications as solid electrolytes for intermediate temperature SOFC.

ACKNOWLEDGMENT

We acknowledge STIC Cochin and NIIST Trivandrum for providing characterization facilities. One of the authors (Sandhya K) acknowledges the University of Kerala for Junior Research Fellowship. We are also grateful to SERB- EMR/2016/007450 for their financial support.

CONFLICT OF INTEREST

The author declares that they have no conflict of interest.

REFERENCES

1. V.V. Kharton, F.M.B. Marques, and A. Atkinson, *Solid State Ion.* 174, 135 (2004).
2. T.H. Etsell and S.N. Flengas, *Chem. Rev.* 70, 339 (1970).
3. N.Q. Minh, *J. Am. Ceram. Soc.* 76, 563 (1995).
4. S.P.S. Badwal and F.T. Ciacchi, *Ionics* 6, 1 (2000).
5. T.S. Zhang, J. Ma, H. Cheng, and S.H. Chan, *Materresbull.* 41, 563 (2006).
6. V.V. Kharton, F.M. Figueiredo, L. Navarro, E.N. Naumovich, A.V. Kovalevsky, A. Yaremchenko, A.P. Viskup, A. Carneiro, F.M.B. Marques, and J.R. Frade, *J. Mater. Sci.* 36, 1105 (2001).
7. M. Mogensen, T. Lindegaard, U.R. Hansen, and G. Mogensen, *J. Electrochem. Soc.* 141, 2122 (1994).
8. S.K. Anirban, T. ProloyDas, and A. Dutta, *Ceram. Int.* 12, 41 (2008).

9. J. Koettgen, S. Grieshammer, P. Hein, and B.O.H. Grope, *Phys. Chem.* 12, 47 (2018).
10. Kerstin Neuhaus, Birgit Gerke, Oliver Niehaus, Sebastian Koops, Timo Hopp, Rainer Pöttgen, and Hans-Dieter Wiemhöfer, *J. Solid State Electrochem.* 20, 2295 (2016).
11. H. Zhang, J. Wang, S. Wang, and Z. Li, *Trans. Nonferrous Met. Soc. China* 17, 565 (2007).
12. Q. Sun, Z. Fu, and Z. Yang, *Ceram. Int.* 44, 3707 (2018).
13. S.J. Hong and A.V. Virkar, *J. Am. Ceram. Soc.* 78, 433 (1995).
14. B.P. Mandal, M. Roy, V. Gover, and A.K. Tyagi, *J. Appl. Phys.* 103, 033506 (2008).
15. M. Stojmenović, S. Bošković, M. Žunić, B. Babić, B. Matović, D. Bajuk-Bogdanović, and S. Menus, *Mat Chem Phys.* 153, 422 (2015).
16. M. Anwar, A. Muchtar, and M.R. Somalu, *Int. J. Appl. Eng. Res.* 11, 9921 (2016).
17. R.K. Lenka, T. Mahata, P.K. Sinha, and P.K. Tyagi, *Solid State Ion.* 181, 262 (2010).
18. R.K. Lenka, T. Mahata, P.K. Sinha, and P.K. Tyagi, *J. Alloys Compd.* 466, 493 (2008).
19. R.F. Tian, F. Zhao, F.L. Chen, and F.R. Xia, *Solid State Ion.* 192, 580 (2011).
20. B. Dietzek, D. Cialla, M. Schmitt, and J. Popp, *Springer Ser. Opt. Sci.* 158, 21 (2010).
21. M. Stojmenović, M.C. Pagnacco, V. Dodevski, J. Gulicovski, M. Žunić, and S. Bošković, *J. Spectro.* 42, 14011 (2016).
22. M. Stojmenović, S. Bošković, S. Zec, B. Babić, B. Matović, D. Bučevac, Z. Dohčević-Mitrović, and F. Aldinger, *J. Alloys Compd.* 507, 279 (2010).
23. M. Stojmenović, M. Žunić, J. Gulicovski, D. Bajuk-Bogdanović, I. Holclajtner-Antunović, V. Dodevski, and S. Menus, *J. Mater. Sci.* 50, 3781 (2015).
24. M. Stojmenović, M.C. Milenković, P.T. Banković, M. Žunić, J.J. Gulicovski, J.R. Pantić, and S.B. Bošković, *Dyes Pigm.* 123, 116 (2015).
25. J. Irvine, T.S. Sinclair, and D.C. West, *Adv. Mater.* 2, 132 (1990).
26. A.K. Jonscher, *Nature* 267, 673 (1977).
27. K. Funke, *Solid State Ion.* 94, 27 (1977).
28. G.B. Balazs and R.S. Glass, *Solid State Ion.* 76, 155 (1995).
29. I.M. Hodge, M.D. Ingram, and A.R. West, *J. Electroanal. Chem.* 74, 125 (1976).
30. N. Jaiswal, S. Upadhyay, D. Kumar, and O. Parkash, *Int. J. Hydrog. Energy* 39, 543 (2014).